nature geoscience

ARTICLES

PUBLISHED ONLINE: 19 DECEMBER 2016 | DOI: 10.1038/NGEO2860

Silicate mineralogy at the surface of Mercury

Olivier Namur[1,2]* and Bernard Charlier[2]

NASA's MESSENGER spacecraft has revealed geochemical diversity across Mercury's volcanic crust. Near-infrared to ultraviolet spectra and images have provided evidence for the Fe^{2+}-poor nature of silicate minerals, magnesium sulfide minerals in hollows and a darkening component attributed to graphite, but existing spectral data is insufficient to build a mineralogical map for the planet. Here we investigate the mineralogical variability of silicates in Mercury's crust using crystallization experiments on magmas with compositions and under reducing conditions expected for Mercury. We find a common crystallization sequence consisting of olivine, plagioclase, pyroxenes and tridymite for all magmas tested. Depending on the cooling rate, we suggest that lavas on Mercury are either fully crystallized or made of a glassy matrix with phenocrysts. Combining the experimental results with geochemical mapping, we can identify several mineralogical provinces: the Northern Volcanic Plains and Smooth Plains, dominated by plagioclase, the High-Mg province, strongly dominated by forsterite, and the Intermediate Plains, comprised of forsterite, plagioclase and enstatite. This implies a temporal evolution of the mineralogy from the oldest lavas, dominated by mafic minerals, to the youngest lavas, dominated by plagioclase, consistent with progressive shallowing and decreasing degree of mantle melting over time.

The surface mineralogy of planetary bodies is one of the most accessible indicators of the processes responsible for the origin and evolution of crustal materials[1–3]. Surface mineralogy was the primary constraint that highlighted the formation of the Moon's anorthosite crust[4,5] and hydrous alteration on Mars[6]. Mercury's surface is made up of secondary volcanic terrains[7–12] with high- and low-Mg regions, consistent with melting of a compositionally heterogeneous mantle[13,14]. Multispectral imaging with the Mercury Dual Imaging System (MDIS) and spectral reflectance measurements with Mercury Atmospheric and Surface Composition Spectrometer (MASCS) revealed the presence of accessory phases[15] such as graphite[16], sulfide minerals[17], as well as surface ice water in polar regions[18]. They also reveal that Mercury's crust contains abundant Fe^{2+}-poor silicate minerals, but spectral data were insufficient to identify these minerals[19]. The MESSENGER spacecraft also included X-Ray (XRS) and Gamma-Ray (GRS) detectors that were used to characterize the elemental composition of Mercury's crust. Mercurian magmas are Mg-rich and Al-, Ca- and Fe-poor compared to terrestrial and lunar material[20,21], and are enriched in alkalis and volatile elements[21–23]. These data, especially in the northern hemisphere where the resolution is the highest, were used to distinguish various geochemical provinces, including the 4.2–4.0 Gyr-old High-Mg (HMg) and Intermediate (IcP-HCT) Plains, the 3.9–3.5 Gyr-old Smooth Plains (SP) and the low- to high-Mg Northern Volcanic Plains (NVP)[21,23].

Crystallization of Mercurian magmas

We have examined XRS chemical maps of Mercury[22,24] and identified average compositions for the various provinces. We experimentally investigated the phase equilibria of five S-free compositions (Supplementary Tables 1 and 2). Experiments were performed from 1,480 to 1,100 °C at 1 kbar under reducing conditions similar to those of Mercury's mantle[25] (~IW-5, IW being the iron–wüstite buffer; see Methods). All compositions fall within the forsterite stability field at low pressure (Fig. 1). For the SiO_2-rich lavas of the NVP, stabilization of forsterite at the expense of orthopyroxene is due to the high Na_2O content of our starting composition (~7 wt%)[26]. The liquidus temperature ranges from 1,440 to 1,290 °C with decreasing MgO content. With decreasing temperature, residual melts become saturated first in

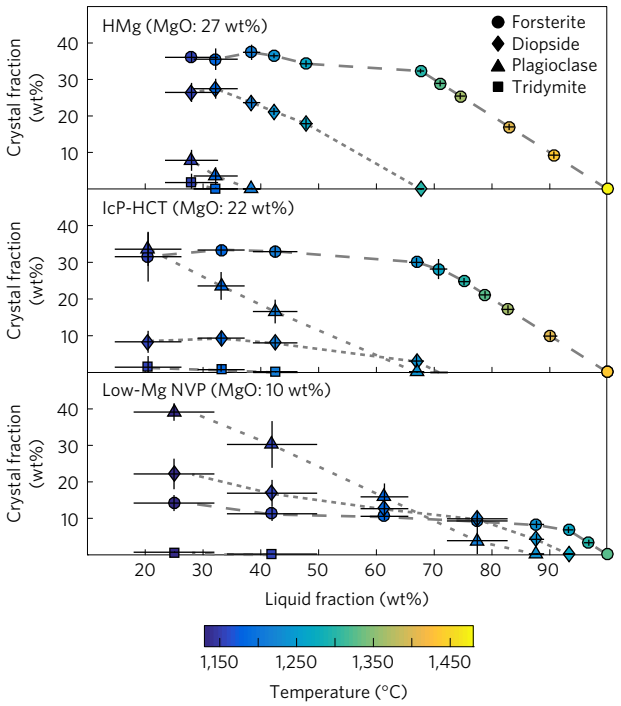

Figure 1 | Evolution of mineral modes (wt%) in experiments on the low-Mg NVP, SP and HMg compositions. Mineral modes in experiments on the High-Mg NVP and SP compositions are given in Supplementary Table 2 (Supplementary Methods). Mineral modes were estimated from mass-balance calculations. Vertical and horizontal bars represent one standard deviation uncertainties (1σ).

[1]Leibniz University Hannover, Institute of Mineralogy, 30167 Hannover, Germany. [2]University of Liège, Department of Geology, 4000 Sart-Tilman, Belgium. *e-mail: o.namur@mineralogie.uni-hannover.de

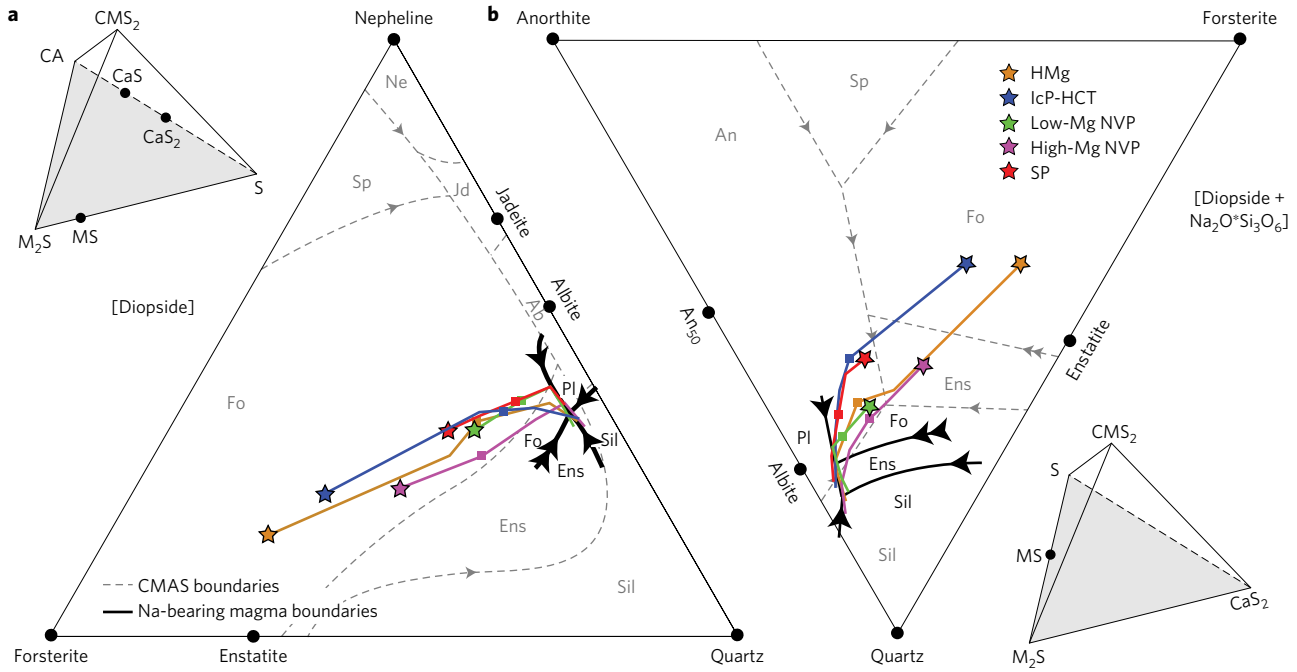

Figure 2 | Representation of the chemical compositions of experimental silicate melts in phase diagrams. a, Projection of experimental melts from diopside onto the plane forsterite–quartz–nepheline. **b**, Projection from diopside + $Na_2O^*Si_3O_6$ onto the plane anorthite–quartz–forsterite. Dashed lines represent low-pressure liquidus boundaries in the CMAS ($CaO–MgO–Al_2O_3–SiO_2$) system (see details in refs 14,25). Thick black lines are liquidus boundaries in a Na-bearing system as determined in this study. Note that the eutectic position with enstatite, forsterite, plagioclase and tridymite is shifted towards the quartz apex and away from the forsterite apex compared to its position in the CMAS system.

diopside, followed by plagioclase, ortho-enstatite and tridymite (Supplementary Fig. 1). At the lowest residual liquid fraction, the Al-poor HMg composition is dominated by forsterite and diopside, with minor enstatite, plagioclase and tridymite. Owing to their Al-rich nature, the IcP-HCT and NVP compositions are dominated by plagioclase but still contain abundant forsterite and diopside. With progressive crystallization, residual liquids become progressively enriched in SiO_2, Al_2O_3 and Na_2O, while MgO continuously decreases (Supplementary Fig. 2). Liquids move away from the forsterite apex towards the nepheline–quartz join in the forsterite–nepheline–quartz phase diagram, and towards the anorthite–quartz join in the anorthite–forsterite–quartz diagram (Fig. 2). At low residual melt fraction, they reach a eutectic point where they are saturated with forsterite, diopside, enstatite, plagioclase and tridymite. During complete solidification, no additional phases are expected to appear. Similar silicate phases would crystallize from S-bearing Mercurian lavas[25,27].

Although explosive volcanism occurred on Mercury[10,28–30], magmatic activity mainly consisted of effusive, hot (1,250–1,520 °C; ref. 25) lava flows with low viscosity[31]. Some of these flows can be followed for more than 200 km[31–33]. Amongst terrestrial planets, Mercury has an unusual temperature distribution[34]. At latitudes above 85°, the temperature is always below 0 °C. At the equator, the maximum temperature ranges from −150 °C during the night to 300 °C during the day. At a depth of 10–20 cm in the regolith, the average temperature ranges from −75 °C in the polar region to 50 °C along the equator. The extreme thermal contrast between Mercurian magmas and the cold regolith is therefore likely to have exerted a major control on the erupting magma cooling at the planet's surface[35].

Basaltic magmas on Earth generally contain a significant crystal cargo dominated by crystals formed in deep-seated magma chambers or by magma decompression during ascent. Our compilation of >1,500 individual mineral mode analyses in plagioclase-saturated basalts, picrites and andesites show that magmas contain 0–70 vol.% crystals with average values of 15, 22 and 37 vol.%, respectively (Supplementary Fig. 3). Once they reach the Earth's surface, magmas can quench rapidly at the top of the lava flow, forming a glassy matrix, but cool more slowly in the flow's interior, forming a fine-grained crystalline matrix surrounding the phenocrysts. On airless planetary surfaces, basaltic magmas are also commonly characterized by a glassy matrix embedded with large phenocrysts[35,36]. On Mercury, the generally cold temperatures both at the surface and at shallow depths in the regolith are likely to result in efficient magma quenching during effusion. Combined with impact melts, the regolith should therefore contain a fair amount of phenocryst-bearing volcanic glass[35]. Rocks originating from deeper parts of lava flows can also be exposed at the surface during crustal reprocessing by meteorite impacts. Slow cooling of these lavas will produce fully crystallized rocks comprising minerals stable at the solidus temperature. It is therefore probable that Mercury's surface contains both phenocryst-bearing glassy rocks and fully crystallized basalts. In the following section, we evaluate the mineralogy of both glass-rich and fully crystallized crusts, although meteorite bombardment is likely to have produced a fine-grained regolith (that is, 50 μm) dominated by glass and crystals.

Mineralogy of lavas

By analogy with basaltic magmatism on Earth, we inferred that glassy rocks on Mercury may contain a range of phenocryst fractions of 15–35 wt% crystals. We used our experimental results to parameterize the residual liquid fraction at the appearance of diopside and plagioclase, the next phases to appear after olivine (Methods and Supplementary Figs 4 and 5). XRS maps from MESSENGER[24] were converted to oxide compositions (Methods and Supplementary Figs 6 and 7). For each composition, we calculated fractionation trends until the crystallinity reached 15, 25 or 35%, and then determined whether or not the residual liquids were saturated in diopside ± plagioclase. From this analysis, several mineralogical provinces can be identified on Mercury's crust

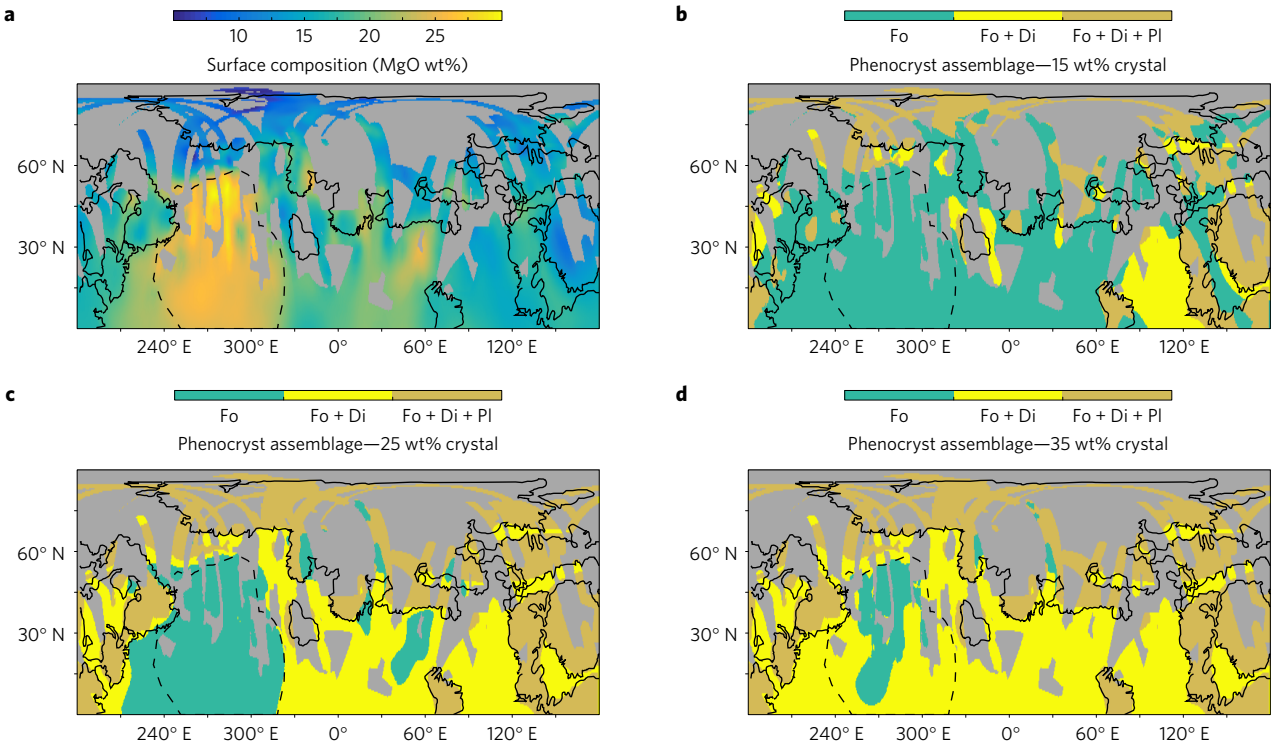

Figure 3 | Maps of chemical composition and mineralogy of crystal-bearing glassy surfaces in the northern hemisphere of Mercury. a, Calculated MgO content of Mercury's secondary volcanic crust (based on XRS and GRS data from MESSENGER[22,24]). **b**, Stable silicate mineralogy for lavas erupting with 15 wt% crystals. **c**, Mineralogy for lavas with 25 wt% crystals. **d**, Mineralogy for lavas with 35 wt% crystals. Thin black lines represent the boundaries of the smooth plains as described in ref. 45 and the black dashed line represents the boundary of the HMg province. Grey pixels are regions for which Ca/Si and S/Si ratios were not measured.

(Fig. 3). In particular, we find that NVP and SP lavas contain a significant proportion of plagioclase, in addition to forsterite and diopside, while IcP-HCT lavas are dominated by forsterite or forsterite + diopside. Lavas from the HMg province, and especially those containing the highest amount of MgO, may contain only forsterite crystals. The presence of plagioclase-bearing lavas in the northern regions of the planet is important for their eruption dynamics. The NVP region comprises the largest lava flows, with some of them reaching a length of more than 200 km (ref. 32). Such large lava flows are commonly interpreted as being produced by a high magma effusivity of 5×10^3 to 6×10^6 m^3 s^{-1}, comparable to magmatic fluxes in continental flood basalts on Earth and in fissure eruptions on Mars[32]. However, a plagioclase load in these lavas would increase the viscosity of the Mercurian lavas by several orders of magnitude (logη: −1, 2 and 5 at a crystallinity of 0, 15 and 30 wt%, respectively[37]). To cover distances in excess of 100 km, the effusion rate of magma in the NVP would therefore need to be extremely high ($>10^7$ m^3 s^{-1}), significantly exceeding the effusion rates observed at the surface of other planets[38].

Mineralogy of crystalline rocks

For rock exposures from deeper portions of lava flows, which are likely to be exposed at the planet surface due to meteorite bombardment, the silicate mineralogy at the solidus and modal proportions can be estimated by mass-balance between the stable phases and the bulk composition of the lava (Methods). This method is also valid if some rocks represent cumulates having crystallized in upper crustal magma chambers. Based on our experimental data, we consider that possible minerals are forsterite, diopside, enstatite, quartz and plagioclase. The first four minerals are pure-Mg endmembers and their compositions do not change with temperature or lava composition (Supplementary Table 1). In contrast, plagioclase is a solid solution between anorthite and albite. In lava flows from metres to tens of metres in thickness[31], cooling is sufficiently fast to produce essentially unzoned groundmass crystals[39]. The composition of plagioclase therefore depends only on the composition of the lava, and essentially on its Ca/Na ratio[40]. We performed mass-balance calculations using the bulk compositions of our experiments and the solidus phases to estimate the composition of plagioclase in the various geochemical provinces on Mercury (Methods). We find that NVP lavas contain albitic plagioclase (An_{17}), consistent with their high Na_2O content (7 wt%)[22], while HMg lavas contain more anorthitic plagioclase (An_{34}), consistent with their high CaO content (7–9 wt%; Supplementary Fig. 6). Other provinces have plagioclase compositions intermediate between NVP and HMg (Supplementary Fig. 8). Once plagioclase composition is identified, the modal mineralogy of each lava composition can be estimated (Fig. 4). The mineralogy at the solidus also demarcates various mineralogical provinces on Mercury's crust. The HMg province has the highest forsterite (>25%) and diopside (>20%) contents, the lowest plagioclase content (<40%) and a relatively low amount of enstatite (<15%). NVP rocks are also rich in forsterite (>10–15%) and diopside (>15%), but contain abundant plagioclase (>50%). In contrast to a previous study[26], our results also indicate they contain abundant quartz. They are peculiar among Mercurian rocks because they do not contain enstatite. However, this is due to the high Na_2O content of these lavas, and an enstatite component is expected if the Na_2O content was increased by thermal migration of Na from the equatorial regions towards the poles[22]. The Intermediate Plains (IcP-HCT) have the highest enstatite content (>25%) and are also fairly enriched in plagioclase (>45%). In the Smooth Plains, the Caloris Basin has the most striking mineralogy, with the highest plagioclase fraction (>60%) in the northern hemisphere and a

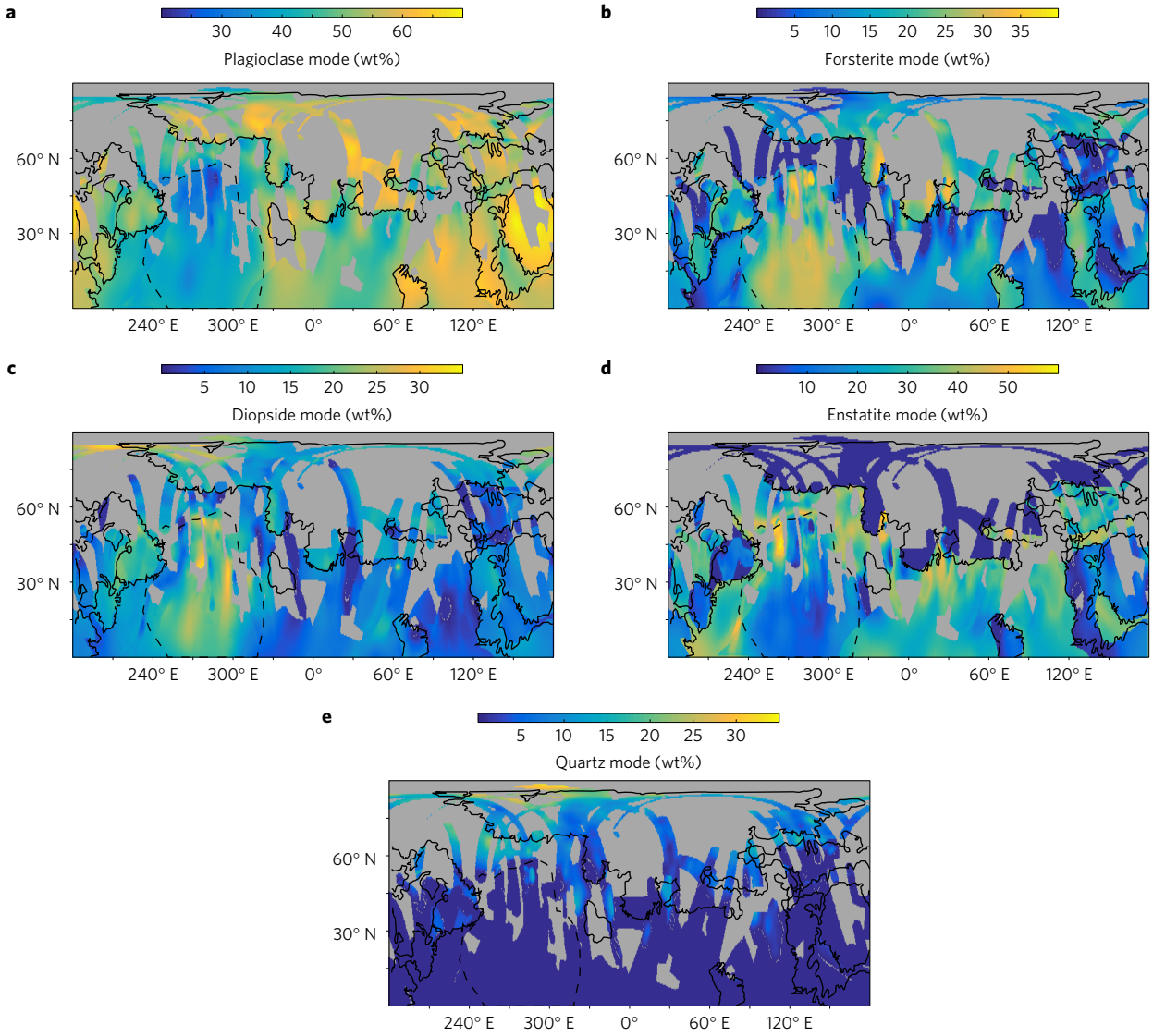

Figure 4 | Mineralogy and mineral modes for a fully crystalline volcanic crust in the northern hemisphere of Mercury. a, Plagioclase mode (wt%). **b**, Forsterite mode (wt%). **c**, Diopside mode (wt%). **d**, Enstatite mode (wt%). **e**, Quartz mode (wt%). See error maps in Supplementary Fig. 9.

low proportion of mafic phases, consisting of forsterite, diopside and enstatite in similar proportions. The plagioclase-rich nature of Caloris may imply that the source of magma has an important crustal component and/or that plagioclase floated to the surface of a large impact melt pool. In any case, the peculiar mineralogy of Caloris supports that this area might be the sole significant portion of tertiary crust on Mercury.

Structure and temporal evolution of the crust

The mineralogical variability that we identified for Mercury's crust has important implications for the physical properties of the crust, particularly its density. Our calculated mineralogy translates to pore-free crustal densities of 2,800–3,150 kg m^{-3}. These densities are similar to previously proposed values[41], but our results show that a non-constant density across the planet should be considered when estimating crustal thickness[41,42]. The densest crust is observed in the forsterite-dominated and plagioclase-poor regions, where crustal density approaches the estimated density of the mantle (3,200–3,300 kg m^{-3}; refs 25,41). In these regions, lower crustal delamination and asthenospheric return are likely to have contributed to high magma productivity. A high density for the HMg province also implies a thicker crust than currently estimated[41,42], which is inconsistent with mantle excavation by a meteorite impact[21] but supports a high degree of mantle melting beneath this region[14]. The presence of >30% of plagioclase in this region also supports the volcanic origin of the HMg rocks. The HMg province on Mercury is therefore not an equivalent to the South Pole–Aitken basin on the Moon where mantle rocks were excavated[43].

The silicate mineralogy at the surface of Mercury is closely related to the geochemical terranes[21]. It also has an obvious relationship to the age of the lavas, as defined by crater size–frequency analyses. Model ages range from 4.2 Gyr for the high-Mg terrane to 3.6–3.5 Gyr for some smooth plains[44]. Secular cooling of the interior of Mercury and the changes of adiabatic mantle melting conditions from deeper and hotter (1,650 °C and 360 km) 4.2 Gyr ago to shallower and cooler (1,410 °C and 160 km) 3.5 Gyr ago (ref. 14) produced lavas successively dominated by forsterite, then forsterite + diopside, and finally forsterite + diopside + plagioclase. The evolution of the mineralogy to a lower-temperature assemblage in the last major volcanic event of the planet (NVP) is consistent with the termination of large-scale magmatic activity 3.5 Gyr ago due to mantle potential temperature becoming lower than the mantle solidus.

Methods

Methods, including statements of data availability and any associated accession codes and references, are available in the online version of this paper.

Received 11 July 2016; accepted 17 November 2016; published online 19 December 2016

References

1. Binzel, R. P. & Xu, S. Chips off of asteroid 4 Vesta: evidence for the parent body of basaltic achondrite meteorites. *Science* **260,** 186–191 (1993).
2. Mustard, J. *et al*. Olivine and pyroxene diversity in the crust of Mars. *Science* **307,** 1594–1597 (2005).
3. Papike, J., Karner, J., Shearer, C. & Burger, P. Silicate mineralogy of martian meteorites. *Geochim. Cosmochim. Acta* **73,** 7443–7485 (2009).
4. Smith, J. V. *et al*. Petrologic history of the Moon inferred from petrography, mineralogy and petrogenesis of Apollo 11 rocks. in *Proc. Apollo 11 Lunar Sci. Conf.* Vol. 1 (ed. Levinson, A. A.) 897–925 (Pergamon Press, 1970).
5. Ohtake, M. *et al*. The global distribution of pure anorthosite on the Moon. *Nature* **461,** 236–240 (2009).
6. Bibring, J. P. *et al*. Global mineralogical and aqueous Mars history derived from OMEGA/Mars Express data. *Science* **312,** 400–404 (2006).
7. Strom, R. G., Trask, N. J. & Guest, J. E. Tectonism and volcanism on Mercury. *J. Geophys. Res.* **80,** 2478–2507 (1975).
8. Fassett, C. I., Kadish, S. J., Head, J. W., Solomon, S. C. & Strom, R. G. The global population of large craters on Mercury and comparison with the Moon. *Geophys. Res. Lett.* **38,** L10202 (2011).
9. Denevi, B. W. *et al*. The evolution of Mercury's crust: a global perspective from MESSENGER. *Science* **324,** 613–618 (2009).
10. Head, J. W. *et al*. Volcanism on Mercury: evidence from the first MESSENGER flyby for extrusive and explosive activity and the volcanic origin of plains. *Earth Planet. Sci. Lett.* **285,** 227–242 (2009).
11. Head, J. W. *et al*. Flood volcanism in the northern high latitudes of Mercury revealed by MESSENGER. *Science* **333,** 1853–1856 (2011).
12. Marchi, S. *et al*. Global resurfacing of Mercury 4.0–4.1 billion years ago by heavy bombardment and volcanism. *Nature* **499,** 59–61 (2013).
13. Charlier, B., Grove, T. L. & Zuber, M. T. Phase equilibria of ultramafic compositions on Mercury and the origin of the compositional dichotomy. *Earth Planet. Sci. Lett.* **363,** 50–60 (2013).
14. Namur, O. *et al*. Melting processes and mantle sources of lavas on Mercury. *Earth Planet. Sci. Lett.* **439,** 117–128 (2016).
15. Murchie, S. L. *et al*. Orbital multispectral mapping of Mercury with the MESSENGER Mercury Dual Imaging System: evidence for the origins of plains units and low-reflectance material. *Icarus* **254,** 287–305 (2015).
16. Peplowski, P. N. *et al*. Remote sensing evidence for an ancient carbon-bearing crust on Mercury. *Nat. Geosci.* **9,** 273–276 (2016).
17. Vilas, F. *et al*. Mineralogical indicators of Mercury's hollows composition in MESSENGER color observations. *Geophys. Res. Lett.* **43,** 1450–1456 (2016).
18. Neumann, G. A. *et al*. Bright and dark polar deposits on Mercury: evidence for surface volatiles. *Science* **339,** 296–300 (2013).
19. Izenberg, N. R. *et al*. The low-iron, reduced surface of Mercury as seen in spectral reflectance by MESSENGER. *Icarus* **228,** 364–374 (2014).
20. Nittler, L. R. *et al*. The major-element composition of Mercury's surface from MESSENGER X-ray spectrometry. *Science* **333,** 1847–1850 (2011).
21. Weider, S. Z. *et al*. Evidence for geochemical terranes on Mercury: global mapping of major elements with MESSENGER's X-Ray Spectrometer. *Earth Planet. Sci. Lett.* **416,** 109–120 (2015).
22. Peplowski, P. N. *et al*. Enhanced sodium abundance in Mercury's north polar region revealed by the MESSENGER Gamma-ray spectrometer. *Icarus* **228,** 86–95 (2014).
23. Peplowski, P. N. *et al*. Geochemical terranes of Mercury's northern hemisphere as revealed by MESSENGER neutron measurements. *Icarus* **253,** 346–363 (2015).
24. Nittler, L. R. *et al*. Global major-element maps of Mercury updated from four years of MESSENGER X-Ray observations. *Proc. Lunar Planet. Sci. Conf.* Vol. XLVII, 1237 (2016).
25. Namur, O., Charlier, B., Holtz, F., Cartier, C. & McCammon, C. Sulfur solubility in reduced mafic silicate melts: implications for the speciation and distribution of sulfur on Mercury. *Earth Planet. Sci. Lett.* **448,** 102–114 (2016).
26. Vander Kaaden, K. E. & McCubbin, F. M. The origin of boninites on Mercury: an experimental study of the northern volcanic plains lavas. *Geochim. Cosmochim. Acta* **173,** 246–263 (2016).
27. McCoy, T. J., Dickinson, T. L. & Lofgren, G. E. Partial melting of the Indarch (EH4) meteorite: a textural, chemical, and phase relations view of melting and melt migration. *Meteorol. Planet. Sci.* **34,** 735–746 (1999).
28. Kerber, L. *et al*. Explosive volcanic eruptions on Mercury: eruption conditions, magma volatile content, and implications for interior volatile abundances. *Earth Planet. Sci. Lett.* **285,** 263–271 (2009).
29. Goudge, T. A. *et al*. Global inventory and characterization of pyroclastic deposits on Mercury: new insights into pyroclastic activity from MESSENGER orbital data. *J. Geophys. Res.* **119,** 635–658 (2014).
30. Thomas, R. J., Rothery, D. A., Conway, S. J. & Anand, M. Long-lived explosive volcanism on Mercury. *Geophys. Res. Lett.* **41,** 6084–6092 (2014).
31. Byrne, P. K. *et al*. An assemblage of lava flow features on Mercury. *J. Geophys. Res.* **118,** 1303–1322 (2013).
32. Hurwitz, D. M. *et al*. Investigating the origin of candidate lava channels on Mercury with MESSENGER data: theory and observations. *J. Geophys. Res.* **118,** 471–486 (2013).
33. Sehlke, A. & Whittington, A. G. Rheology of lava flows on Mercury: an analog experimental study. *J. Geophys. Res.* **120,** 1924–1955 (2015).
34. Vasavada, A. R., Paige, D. A. & Wood, S. E. Near-surface temperatures on Mercury and the Moon and the stability of polar ice deposits. *Icarus* **141,** 179–193 (1999).
35. Grove, T. L. & Krawczynski, M. J. Lunar mare volcanism: where did the magmas come from? *Elements* **5,** 29–34 (2009).
36. Walker, D., Kirkpatrick, R., Longhi, J. & Hays, J. Crystallization history of lunar picritic basalt sample 12002: phase-equilibria and cooling-rate studies. *Geol. Soc. Am. Bull.* **87,** 646–656 (1976).
37. Chevrel, M. *et al*. Lava flow rheology: a comparison of morphological and petrological methods. *Earth Planet. Sci. Lett.* **384,** 109–120 (2013).
38. Gregg, T. K. P. & Fink, J. H. Quantification of extraterrestrial lava flow effusion rates through laboratory simulation. *J. Geophys. Res.* **101,** 16891–16900 (1996).
39. Philpotts, A. R. & Dickson, L. D. The formation of plagioclase chains during convective transfer in basaltic magma. *Nature* **406,** 59–61 (2000).
40. Namur, O., Charlier, B., Toplis, M. J. & Vander Auwera, J. Prediction of plagioclase-melt equilibria in anhydrous silicate melts at 1-atm. *Contrib. Mineral. Petrol.* **163,** 133–150 (2012).
41. Padovan, S., Wieczorek, M. A., Margot, J.-L., Tosi, N. & Solomon, S. C. Thickness of the crust of Mercury from geoid-to-topography ratios. *Geophys. Res. Lett.* **42,** 1029–1038 (2015).
42. James, P. B., Zuber, M. T., Phillips, R. J. & Solomon, S. C. Support of long-wavelength topography on Mercury inferred from MESSENGER measurements of gravity and topography. *J. Geophys. Res.* **120,** 287–310 (2015).
43. Pieters, C. M., Tompkins, S., Head, J. & Hess, P. Mineralogy of the mafic anomaly in the South Pole-Aitken Basin: implications for excavation of the lunar mantle. *Geophys. Res. Lett.* **24,** 1903–1906 (1997).
44. Byrne, P. K. *et al*. Widespread effusive volcanism on Mercury likely ended by about 3.5 Ga. *Geophys. Res. Lett.* **43,** 7408–7416 (2016).
45. Denevi, B. W. *et al*. The distribution and origin of smooth plains on Mercury. *J. Geophys. Res.* **118,** 891–907 (2013).

Acknowledgements

This research was carried out with financial support from a Marie Curie Intra-European Fellowship (SULFURONMERCURY-327046) to O.N. and the Belspo BRAIN-be program (BR/143/A2/COME-IN). O.N. also acknowledges support from the Belgian Fund for Scientific Research—FNRS for a position of Postdoctoral Researcher (Grant 1.B.341.16). B.C. is a Research Associate of the Belgian Fund for Scientific Research—FNRS. L. Nittler is thanked for providing the most recent XRS maps of Mercury. B. Mandler and V. Honour are thanked for careful editing of the manuscript.

Author contributions

O.N. and B.C. designed the project. O.N. conducted the experiments and modelling. O.N. and B.C. interpreted the results and prepared the manuscript.

Additional information

Supplementary information is available in the online version of the paper. Reprints and permissions information is available online at www.nature.com/reprints. Correspondence and requests for materials should be addressed to O.N.

Competing financial interests

The authors declare no competing financial interests.

Methods

Calculation of Mercurian surface compositions. The surface composition of the Mercurian volcanic crust (Supplementary Table 3) was calculated using the most recent maps produced from MESSENGER XRS data[24]. We focused on the northern hemisphere, where the spatial resolution of MESSENGER measurements is the highest and where ~70% of the surface was covered. We combined individual maps of Mg/Si, Ca/Si, Al/Si and S/Si, and worked only on pixels for which those four ratios were measured. This method allows us to investigate only some parts of the northern hemisphere because the Ca/Si and S/Si maps are not complete. We produced >79,000 compositional groups of four pixels (0.5° latitude × 0.5° longitude) that we converted to chemical compositions (SiO_2, Al_2O_3, MgO, CaO, S). Each pixel group was assigned to the geochemical province in which it is located (NVP, SP, IcP-HCT, HMg), to which we attributed specific concentrations of minor elements (Ti, Mn, K[23]). For Na, we considered that NVP lavas have high Na_2O contents (Na/Si = 0.20; ~7 wt% Na_2O), SP lavas have intermediate Na_2O contents (Na/Si = 0.14; ~5 wt% Na_2O) and IcP-HCT and HMg lavas have lower Na_2O contents (Na/Si = 0.06; ~2 wt% Na_2O (ref. 22)). Final chemical analyses were normalized to 100 wt%. The interested reader is referred to ref. 22 for a discussion of Na_2O contents in Mercurian lavas (including secondary thermal migration of Na) and to ref. 26 for the effect of Na on the mineralogy of Mercurian lavas.

To calculate the silicate mineralogy of Mercurian lavas, we recalculated S-free magma compositions and assumed that S forms complexes with Mg and Ca in the silicate melt[25]. Experiments in Fe-free systems at reducing conditions (<IW-5[25]) show that sulfide saturation produces sulfide melt globules with an average composition of $(Mg_{0.8}Ca_{0.2})S$[25]. We therefore inferred that S forms complexes with a similar composition in the silicate melt and recalculated S-free silicate melt compositions by changing the Ca and Mg contents according to the bulk S content measured by MESSENGER. Results are shown in Supplementary Fig. 6 (Supplementary Methods).

Starting compositions and experimental methods. Using calculated surface compositions (Supplementary Fig. 6), we identified five starting compositions representing average compositions for the various geochemical provinces (Low-Mg NVP, High-Mg NVP, SP, IcP-HCT, HMg[23]). Silicate starting compositions for experiments were produced from high-purity commercially purchased oxides (SiO_2, TiO_2, Al_2O_3, MgO, MnO, NiO, Cr_2O_3) and carbonates ($CaCO_3$, Na_2CO_3, K_2CO_3). Silicate components were mixed with a metal mixture ($Fe_{90}Si_{10}$) to set the oxygen fugacity to highly reducing conditions relevant to Mercurian magmas (<IW-5[25]). The ground starting material was packed into 3 mm (inner diameter) graphite capsules with top lids, and dried for 24 h at 120–150 °C. Experiments were performed at 1 kbar in large-volume internally heated pressure vessels (IHPV) at the University of Hannover. Argon was used as the pressure medium. The graphite capsules were placed into an outer Pt jacket (inner diameter = 4 mm) welded shut with bottom and top Pt lids. Temperature was controlled using four S-type thermocouples ($Pt\text{-}Pt_{90}Rh_{10}$). Experiments were ramped at 1 °C s^{-1} to the final temperature. For experiments at the lowest temperatures (<1,200 °C), experiments were first heated to 1,300 °C, kept at this temperature for 1 h, and then cooled to the final temperature at a rate of 2 °C s^{-1}. The temperature gradient across the sample was less than 5 °C. Quenching (~150 °C s^{-1}) was performed by dropping the sample onto a cold (~25 °C) copper block. To reach equilibrium, the run durations of the experiments were between 4 and 108 h. Such long runs in IHPV impose us to work on S-free compositions but S is not likely to have any significant effect on low-pressure phase equilibria[14,25,27].

Analytical methods. Experimental charges were analysed with a CAMECA SX100 electron microprobe analyser (EMPA) at the University of Hannover. Analyses were performed with an accelerating voltage of 15 kV. For glasses in near-liquidus experiments, we used a beam current of 8 nA and a defocused beam diameter of 10 µm. For glasses in experiments closer to the solidus, we used a beam current of 4 nA. For metals, we used a beam current of 15 nA and a defocused beam diameter of 2–20 µm. Mineral analyses were performed with a beam current of 15 nA and a focused beam (1 µm diameter). Counting time on peaks was 15–20 s (7.5–10 s for background) for each element. For glasses and minerals, we used the following standards for Kα X-ray line calibration: albite for Na, orthoclase for K, wollastonite for Si and Ca, TiO_2 for Ti, Fe_2O_3 for Fe, MgO for Mg, Mn_3O_4 for Mn and Cr_2O_3 for Cr. For metal melts, we used pure metal Mg, Si, Fe, Cr, Ni, Mn, wollastonite for Ca and TiO_2 for Ti. Raw data were corrected with the CITZAF software.

Calculation of oxygen fugacity. The presence of silicate melt (Sil) and Fe-rich metal alloy (Met) in our experiments constrain the intrinsic oxygen fugacity (f_{O_2}) of the system by the equilibrium:

$$Fe_{Met} + \frac{1}{2}O_2 = FeO_{Sil} \quad (1)$$

where the f_{O_2} of the experiment (Ex) can be expressed relative to the f_{O_2} of the iron–wüstite (Fe–FeO; IW) oxygen fugacity buffer by the following equations:

$$\Delta IW = \log f_{O_{2;Ex}} - \log f_{O_{2;IW}} \quad (2)$$

$$\Delta IW = 2\log\left(\frac{a_{FeO}^{Sil}}{a_{Fe}^{Met}}\right) = 2\log\left(\frac{X_{FeO}^{Sil}\gamma_{FeO}^{Sil}}{X_{Fe}^{Met}\gamma_{Fe}^{Met}}\right) \quad (3)$$

where a_{FeO} is the activity of FeO in the silicate melt, γ_{FeO} is the activity coefficient of FeO, X_{FeO} is the molar fraction of FeO, a_{Fe} is the activity of Fe in the metal alloy, γ_{Fe} is the activity coefficient of Fe, X_{Fe} is the molar fraction of Fe. We considered a value of 1.5 for γ_{FeO}, which corresponds to the average value of two studies having investigated this parameter[46,47]. γ_{Fe} was calculated using the interaction parameter formalism (ε-approach[48–50]), which takes into account the non-ideal interaction between all components in the Fe-rich metal alloy. Interaction parameters (ε) and activity coefficients of any element infinitely diluted in the Fe-rich metal alloy (γ^0) were selected from various studies[49–52] and were extrapolated from 1,873 K (reference temperature) to the temperature of the experiment following the procedure of ref. 49.

For most experiments, the FeO content of the silicate melt is too low to be accurately measured by electron microprobe, which results in poorly estimated values for a_{FeO} and therefore f_{O_2} cannot be calculated. We have also calculated the f_{O_2} of the experiments using the following equilibrium[53]:

$$Si^{Met} + O_2 = SiO_2^{Sil} \quad (4)$$

which is described by the following thermodynamic equation:

$$\Delta G = 0 = \Delta G^0 + RT\ln K_{eq} \quad (5)$$

with

$$K_{eq} = \frac{a_{Si}^{Met} f_{O_2}}{a_{SiO_2}^{Sil}} \quad (6)$$

and

$$\Delta G^0 = \Delta H_r^0 - T\Delta S_r^0 + \int \Delta V\,dP \quad (7)$$

leading to

$$f_{O_2} = e^{\frac{-\Delta G^0}{RT}} \frac{a_{SiO_2}^{Sil}}{a_{Si}^{Met}} \quad (8)$$

where $a_{SiO_2}^{Sil}$ ($X_{SiO_2}\gamma_{SiO_2}$) is the activity of SiO_2 in the silicate melt, a_{Si}^{Met} ($X_{Si}\gamma_{Si}$) is the activity of Si in the Fe-rich metal allow, ΔG^0 is the free energy change for equation (4) at standard conditions, ΔH_r^0 is the enthalpy change of the reaction, ΔS_r^0 is the entropy change of the reaction, ΔV is the volume change, R is the gas constant, T is temperature and P is pressure. In our calculations, we assumed $a_{SiO_2}^{Sil} \approx 1$ and calculated γ_{Si} using the ε-approach. ΔH_r^0, ΔS_r^0 and ΔV were calculated using data from ref. 54. The f_{O_2} of the experiment is expressed relative to IW by equation (2), in which $\log f_{O_{2;IW}}$ is calculated as follows[55,56]:

$$\log f_{O_{2;IW}} = 6.471 - \frac{26{,}834}{T} + 0.055\frac{P-1}{T} \quad (9)$$

Silicate liquidus assemblages. We used our experimental results to parameterize the diopside saturation surface in Mercurian magmas. Using our experimental results together with ~250 experiments in the CMAS (CaO–MgO–Al_2O_3–SiO_2) and CMASN (CaO–MgO–Al_2O_3–SiO_2–Na_2O) systems, we developed an expression to predict the liquidus temperature of Mercurian magmas. We adopted a Gibbs-phase-rule-inspired empirical model[57]. Experiments in the CMAS and CMASN systems have four to five components and are usually saturated with forsterite, and/or enstatite, diopside, feldspar and spinel. We therefore restricted our variables to two to five compositional parameters. After extensive searching, we found that liquidus temperatures can be accurately determined using a set of liquid composition parameters (MgO wt%, Na_2O wt%, MgO/(MgO + SiO_2), $Al_2O_3/(Al_2O_3 + SiO_2)$ and $Na_2O/(Na_2O + CaO)$; see details in the caption of Supplementary Fig. 4). Based on experiments saturated in diopside, we also developed an expression that describes the change in composition and temperature of liquids saturated in diopside (ref. 57; see details in the caption of Supplementary Fig. 5). We used compositional parameters identical to those used to calculate liquidus temperatures. Liquids start crystallizing diopside when they hit the calculated diopside saturation surface. According to our models, diopside appears when the liquidus temperature of the melt is identical to the calculated temperature of diopside saturation. We do not have a sufficient number of experiments

saturated in plagioclase to accurately determine the plagioclase saturation surface. However, we observed that for all investigated compositions, the liquid becomes saturated in plagioclase when the liquidus temperature is below 1,200 °C and the Al_2O_3 content of the equilibrium melt is higher than 14 wt%. We therefore used these two criteria to define the saturation of plagioclase in Mercurian melts.

To predict the stable mineral phases in Mercurian magmas as a function of crystallinity (for example, 15, 25 and 35 wt%; Fig. 3), we used fractional crystallization models. We started by fractionating forsterite (first liquidus phase for all investigated compositions) by steps of 1 wt%. After each step of fractionation, we checked if the liquid was also saturated in diopside ± plagioclase. For diopside, we calculated the liquidus temperature of the magma (equation given in the caption of Supplementary Fig. 4) and the temperature of diopside saturation (equation given in the caption of Supplementary Fig. 5). When both temperatures agreed to within 15 °C (average error for both models), we considered the liquid to be saturated in diopside. After diopside saturation, we kept fractionating forsterite and diopside by steps of 1 wt%. We used our experiments to estimate realistic cotectic proportions in magmas saturated with forsterite and diopside, and found a forsterite:diopside ratio of 1:2. After each fractionation step, we calculated the liquidus temperature and the residual liquid composition. When our criteria of plagioclase saturation were met, we considered the liquid to be saturated in plagioclase. It has been shown that high-temperature phase equilibria in S-free and S-bearing systems are identical[25]. The choice not to include S in our experiments has therefore no effect on our prediction of liquidus phases and the mineral assemblages shown in Fig. 3.

To predict the stable phases at the solidus temperature of Mercurian magmas (Supplementary Table 3), we performed a mass-balance calculation between each compositional group of four pixels (Supplementary Figs 6 and 7) and the experimental mineral phases. Based on our experiments closest to the solidus for each starting composition, we made the initial assumption that lavas on Mercury may have plagioclase, quartz, forsterite, enstatite and diopside as stable phases. In the calculations, we used average compositions of all our microprobe measurements for forsterite, diopside and enstatite. We assumed that quartz is 100 wt% SiO_2. For plagioclase, we used a different composition for each geochemical province. Because our experiments do not unambiguously constrain the plagioclase composition at the solidus temperature, we also estimated it by mass-balance calculation between our experimental starting compositions (representing the average composition of each province) and stable silicate phases. For each set of calculation, plagioclase was allowed to vary from anorthite to albite. The estimated plagioclase composition at the solidus corresponds to the plagioclase composition for which we obtained the best mass-balance fit (lowest values of the sum of squared residuals (r^2; see details in Supplementary Fig. 8). We assumed that phase equilibria at the solidus in S-bearing magmas of Mercury are identical to those observed in our S-free experiments[25,27].

Data sources. Chemical MESSENGER data used to generate Figs 3 and 4 were calculated from the maps published by L. Nittler (ref. 24). JPEG files were made available to the authors by L. Nittler. Raw MESSENGER XRS data are available from Geoscience Node website, Washington University of St. Louis (http://pds-geosciences.wustl.edu/missions/messenger/xrs.htm).

Code availability. The Matlab computer code used to generate Fig. 3 is a simple Rayleigh fractionation model. Raw data and equations used in the codes can be found in Supplementary Methods. The code used to generate Fig. 4 is the 'lsqnonneg' function of the Matlab Statistical Toolbox. All codes can be found at: http://labos.ulg.ac.be/geopetro/people/olivier-namur.

Data availability. The authors declare that the data supporting the findings of this study are available within the article and its Supplementary Information files. The experimental starting compositions and experimental results are given in Supplementary Data Tables 1 and 2. Mercurian lava compositions calculated from MESSENGER measurements and the calculated solidus mineralogy are given in Supplementary Data Table 3.

References

46. Holzheid, A., Palme, H. & Chakraborty, S. The activities of NiO, CoO and FeO in silicate melts. *Chem. Geol.* **139,** 21–38 (1997).
47. O'Neill, H. S. & Mavrogenes, J. A. The sulfide capacity and the sulfur content at sulfide saturation of silicate melts at 1400 °C and 1 bar. *J. Petrol.* **43,** 1049–1087 (2002).
48. Ma, Z. Thermodynamic description for concentrated metallic solutions using interaction parameters. *Metall. Mater. Trans. B* **32,** 87–103 (2001).
49. Wade, J. & Wood, B. J. Core formation and the oxidation state of the Earth. *Earth Planet. Sci. Lett.* **236,** 78–95 (2005).
50. Corgne, A., Keshav, S., Wood, B. J., McDonough, W. F. & Fei, Y. Metal-silicate partitioning and constraints on core composition and oxygen fugacity during Earth accretion. *Geochim. Cosmochim. Acta* **72,** 574–589 (2008).
51. Bouchard, D. & Bale, C. W. Simultaneous optimization of thermochemical data for liquid iron alloys containing C, N, Ti, Si, Mn, S, and P. *Metall. Mater. Trans. B* **26,** 467–484 (1995).
52. Tuff, J., Wood, B. J. & Wade, J. The effect of Si on metal-silicate partitioning of siderophile elements and implications for the conditions of core formation. *Geochim. Cosmochim. Acta* **75,** 673–690 (2011).
53. Cartier, C. *et al*. Experimental study of trace element partitioning between enstatite and melt in enstatite chondrites at low oxygen fugacities and 5 GPa. *Geochim. Cosmochim. Acta* **130,** 167–187 (2014).
54. Robie, R. A. & Hemingway, B. S. Thermodynamic properties of minerals and related substances at 298.15 K and 1 bar pressure and at higher temperatures. *USGS Bull.* **2131,** 1–461 (1995).
55. Huebner, J. S. in *Research Techniques for High Pressure and High Temperature* (ed. Ulmer, G. C.) 123–177 (Springer, 1971).
56. Myers, J. T. & Eugster, H. P. The system Fe–Si–O: oxygen buffer calibrations to 1,500 K. *Contrib. Mineral. Petrol.* **82,** 75–90 (1983).
57. Grove, T. L., Kinzler, R. J. & Bryan, W. B. in *Mantle Flow and Melt Generation at Mid-Ocean Ridges* (eds Phipps Morgan, J., Blackman, D. & Sinton, J.) 281–310 (American Geophysical Union, 1992).